

Quantification of Hepatic Iron Overload using MRI

Sruthi Susan Kuriakose
Iron Group (Supervisor: Ahmed Karam Eldaly)
University College London
sruthi.kuriakose.23@ucl.ac.uk

1 ABSTRACT

Treatment modalities for hemoglobinopathies such as Thalassemia and Sickle Cell Disease frequently necessitate interventions that cause patients to have iron overload, a condition with significant clinical implications if not promptly identified. Traditionally, the assessment of iron overload has relied on liver biopsy, an invasive approach which poses significant patient risks. In this study, we explore the the potential of quantitative MRI techniques as a non-invasive alternative for assessing iron overload, with a particular focus on the application of the Simple Exponential Model for estimating $T2^*$ values, which correlate well with iron concentration. Specifically, we focus on implementing the model using the Alternating Direction Method of Multipliers (ADMM) algorithm and Total Variation method. Validation of this model on a phantom dataset and a dataset comprising four patients has demonstrated its efficacy in accurately determining $T2^*$ values. This suggests that MRI-based quantification could serve as a reliable and non-invasive method for the quantification of iron overload in patients with these conditions.

2 INTRODUCTION

Iron metabolism is tightly regulated within the human body, maintaining a delicate balance between absorption and elimination to prevent both deficiency and overload. Under normal conditions, the concentration of iron within the body is kept within a strict homeostatic window, with daily dietary iron absorption matching the rate of iron loss.[1] However, disruptions in this balance, through mechanisms such as increased intestinal absorption or chronic blood transfusions required for conditions like thalassemia and sickle cell disease can lead to systemic iron overload. This condition is marked by the accumulation of free iron in cellular tissues, which is highly toxic and can cause significant cellular and tissue damage. Accumulation of iron can affect the endocrine glands, liver, and heart, leading to severe complications including growth retardation, endocrine disorders, liver cirrhosis, heart failure, arrhythmias, and cardiac death. Such overload, particularly in the liver — the body's primary iron storage organ — is of significant clinical concern, as it can lead to a host of complications, including organ failure and increased mortality risk. Consequently, it becomes imperative to assess the extent of iron overload to facilitate effective removal via chelation therapy.

The traditional method of quantifying liver iron concentration, liver biopsy, although considered the gold standard, poses risks due to its invasiveness, cost, and potential sampling errors. This highlights the need for non-invasive, accurate, and reliable methods to assess liver iron concentration, thereby facilitating early detection, monitoring, and initiation of chelation therapy to prevent the adverse effects of iron overload. While serum markers including serum iron, transferrin, and ferritin offer a non-invasive, cost-effective means for assessing body iron stores, their accuracy is often compromised by systemic conditions such as malignancy or inflammatory states.[1] Furthermore, the correlation between iron overload and serum ferritin levels has shown inconsistency, partly

attributed to the use of subcutaneous fat as a reference in patients who are excessively thin or those who have received red blood cell transfusions, leading to misleading interpretations of liver signal loss. [2]

Magnetic Resonance Imaging (MRI) has been shown to be a promising non-invasive technique for the assessment of liver iron concentration (LIC). Bondestam et al [2] showed the correlation between the reduction of the MR signal intensity of the liver and the amount of transfused packed red cell units in patients with haematological malignancies, exhibiting the technique's clinical relevance. The principle underlying MRI-based quantification is the impact of iron on the MRI signal, particularly in how iron being paramagnetic, affects tissue susceptibility to the magnetic field and shortens the relaxation times (T1, T2, and T2*) of the MRI signal. This shortening translates into a darker appearance of the liver on T2*-weighted images, offering a direct quantitative measure of iron accumulation. T2* relaxation time, a variant of the transverse relaxation time T2, offers increased sensitivity to the presence of iron as it accounts for both microscopic and macroscopic magnetic field distortions caused by iron deposition. T2 only reflects the microscopic field distortions. Moreover, T2* imaging can be performed relatively quickly, making it more practical for clinical use compared to the longer scan times required for T2 imaging.

There are a few MRI techniques that have been developed and validated to quantify LIC: signal intensity ratio (SIR), R2-based relaxometry, and R2*-based relaxometry. [3] According to some authors [3], "the most practical method with the strongest level of evidence for accurate and reproducible quantification of LIC" is the confounder-corrected R2*-based LIC quantification, with 3T-imaging more sensitive to the presence of iron. This method involves fitting the average signal intensity at different echo times to an exponential decay model to obtain the R2* parameter, which is indicative of the liver iron concentration.

(Ibrahim et al.) [4] scrutinized the impact of methodological choices; various fitting models and signal calculation methods on the precision of T2* measurements in the context of MRI. The study rigorously evaluates the implications of employing single-exponential (EXP), bi-exponential (BEXP), and exponential-plus-constant (CEXP) models, alongside pixel-wise (MAP), average (AVG), and median (MED) approaches for signal computation. They calibrated phantom experiments, and conducted assessments on nine patients with sickle cell disease using a 3 Tesla MRI system, and they recommend the CEXP model and AVG method due to simpler implementation and less influence to variances in selected analysis regions.

However, challenges remain in optimizing these techniques for accurate liver iron measurement. The variability in signal decay captured by MRI can be analyzed using different models, such as single-exponential, bi-exponential, and exponential-plus-constant models, each accounting for the tissue characteristics and presence of iron differently. Moreover, these models often face limitations, including sensitivity to noise and the need for adjustments to account for varying tissue characteristics.

We first describe three of the models used in literature.

1. Single-Exponential Model (SEXP)

$$s = a \exp(-rt) \quad [1]$$

s is measured signal intensity,

t = TE is time to echo vector,

a is the initial signal intensity expected at TE = 0,

r denotes the T2* value

The signal intensity s in these images decays exponentially with echo time (TE). The limitations of this model is that it assumes uniform iron concentration within each tissue voxel

2. Shifted Single-Exponential Model

$$s = a \exp(-rt) + c \quad [2]$$

This addresses the limitations of the single-exponential model; here, constant c is added to account for long T2* components.

3. Bi-Exponential model

$$s = a \exp(-r_1 t) + b \exp(-r_2 t) \quad [3]$$

This model also addresses the limitations of the single-exponential model; the two components modelled include an iron-dense, short-T2* component and an iron-sparse, long-T2* component.

In our study, we aim to create a quick and reliable general framework for estimating T2* values from T2*-weighted MRI images, employing the single-exponential model for calculation.

The Levenberg Marquardt fitting algorithm is also an established algorithm for the assessment of iron overload in liver by T2* MRI.[5] It is an iterative optimization technique that combines the concepts of gradient descent and the Gauss-Newton method to solve non-linear least squares problems. In each iteration, the Levenberg-Marquardt algorithm updates the parameters based on a linear approximation of the error function, using a combination of the Jacobian matrix (Gauss-Newton method) and the gradient of the error (Gradient Descent). The algorithm introduces a factor that adjusts the step size of each iteration: when the factor is high, the algorithm behaves more like gradient descent, taking small, cautious steps; when the factor is low, it acts more like the Gauss-Newton method, taking larger steps.

3 METHODS

Single-Exponential Model (SEXP)

Our study focuses on the single-exponential decay function defined in Equation 1 to correlate T2*-weighted MRI images with liver iron concentration. Given the sequence of images acquired at different echo times (TEs), our objective is to estimate a T2* map, revealing the T2* value for each pixel. To compute this for each pixel, we must estimate a and r which represent the signal intensity at TE=0, and the inverse of the T2* value respectively. This can be achieved by minimizing the difference between the observed signal intensities and the ones predicted by our model across all echo times, framed as the following optimization problem.

$$\min_{a,r} \frac{1}{2} \sum_{n=1}^N |S - a \exp(-rt)|_2^2 \quad [4]$$

Known variables in this scenario include the signal intensity ' S ' at various TEs ' t ', and we aim to estimate a and r to derive the signal intensity at TE=0 and the T2* value.

Total Variation

This formulation presents an ill-posed inverse problem because multiple combinations of 'a' and 'r' can result in the same measured value of 's'. To counteract this, we regularize the problem by incorporating a **Total Variation (TV)** prior, which is based on the assumption that the images are piecewise constant. This assumption holds in our case of MRIs because of the physical properties of the biological tissues such that they generally exhibit uniform signal intensity within a given region but can change abruptly at the boundaries of different anatomical structures. Total Variation regularization enhances the accuracy of edge detection and noise reduction by promoting sparsity in the gradient of the image, effectively smoothing out the areas within the regions while preserving the sharp edges between them.

$$\min_{a,r} \frac{1}{2} \sum_{n=1}^N |S - a \exp(-rt)|_2^2 + \lambda_1 |a|_{TV} + \lambda_2 |r|_{TV} \quad [5]$$

However, the inclusion of the TV prior makes the problem non-smooth and hence, standard gradient-based methods for finding 'a' and 'r' are inapplicable.

Variable Splitting and Lagrangian Methods:

Since the non-differentiability of the TV term requires us to adjust our optimization strategy, we employ variable splitting to separate the likelihood, or data fidelity term, from the regularization terms. In our approach, we introduce auxiliary variables 'g' equated to 'a' and 'f' to 'r', effectively decoupling the data fidelity from regularization. The reformulated problem is addressed through an Augmented Lagrangian approach[6], as seen in equation 6, which introduces Lagrange multipliers h1 and h2.

$$\min_{a,r} \frac{1}{2} \sum_{n=1}^N |S - a \exp(-rt)|_2^2 + \lambda_1 |g|_{TV} + \lambda_2 |f|_{TV} + \frac{\eta}{2} |a - g - h_1|_2^2 + \frac{\eta}{2} |r - f - h_2|_2^2 \quad [6]$$

Alternating Direction Method of Multipliers (ADMM):

To solve the augmented problem, we employ the Alternating Direction Method of Multipliers (ADMM), an iterative optimization algorithm that updates a and r, and the auxiliary variables in succession while progressively adjusting the Lagrange multipliers. This method allows for the efficient minimization of each sub-problem and ensures convergence.

Solve for 'a', 'r', 'g', and 'f' separately involves grouping related terms and solving for the unknowns by setting their derivatives to zero.

The solution for the update equation of a is given in equation 7.

$$a = [\exp(-rt)^T \exp(-rt) + \eta]^{-1} [s \exp(-rT)^T + \eta(g + h_1)] \quad [7]$$

r can be updated using Gradient descent

$$r^{k+1} = r^k - \Delta \frac{\partial H}{\partial r} \quad [8]$$

$$\frac{\partial H}{\partial r} = a (t \odot \exp(-rT)^T [S - a \exp(-rT)]) + \eta(r - f - h_2) \quad [9]$$

For the minimization over g using $\min_g \frac{\eta}{2} |a - g - h_1|_2^2 + \lambda_1 |g|_{TV}$ and minimization over f using $\min_f \frac{\eta}{2} |r - f - h_2|_2^2 + \lambda_2 |f|_{TV}$, we use the Chambolle algorithm[7],

$$g \sim \text{Chambolle} \left(a - h_1, \frac{\lambda_1}{\eta} \right), f \sim \text{Chambolle} \left(r - h_2, \frac{\lambda_2}{\eta} \right) \quad [10]$$

which is effective in solving the TV minimization problem

ADMM Algorithm: At each update step, we optimize for one of the variables while keeping the others constant. After minimizing the four variables a , r , g and f , we update the Lagrange multipliers. Iterate until convergence.

By iterating through this process, we converge on a solution that provides a robust estimate of a and r values which can be used to derive $T2^*$ from the image data.

Validation of Model on Synthetic Data:

A synthetic dataset is generated to simulate signal decay over a sequence of 12 images at varying echo times (TE), for four distinct regions with different initial signal intensities. This simulation mirrors the decay patterns associated with specific $T2^*$ relaxation times, serving as the ground truth for these regions. The model's validation involves comparing the $T2^*$ values estimated from the phantom data against these known ground truth values. The model is also tested on addition of Gaussian noise of zero mean and a variance of 10 to the synthetic data.

Testing of Model on Patient Dataset:

Four subjects diagnosed with sickle cell disease (age: 38 ± 12 years) underwent abdominal in-vivo imaging on a 3Tesla Siemens Skyra MRI system. Images were captured using an 8-echo gradient echo (GRE) sequence, with echo times (TEs) spanning from 1 to 16.4ms in equal increments.



Figure 1: Sequence of liver images of different time to echo, of a patient with mild iron overload.

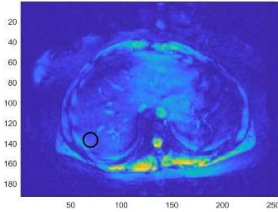


Figure 2: Selected ROI

The imaging protocol employed a repetition time (TR) of 5200 milliseconds, a 192×256 matrix, a bandwidth of 1776 Hz/pixel, flip angle 20, slice thickness 10 mm, and a patient size-dependent field view. In a single end expiration breath-hold, Images of a mid-liver axial slice was acquired. The $T2^*$ -weighted images, as illustrated in Figure 1, exhibit the increasing decay of liver signal intensity with increased TE. The liver's heterogeneous iron distribution, susceptibility to artifacts, and the presence of blood vessels contribute to the variability of $T2^*$ values in different liver regions. As a benchmark for iron content, since biopsy samples were not part of the patients' standard care, we obtain the $T2^*$ reference values from a 4 cm^2 circular region of interest (ROI) positioned centrally within the liver's right lobe using the $T2^*$ mapping software (which applies single-exponential model) integrated into the MRI system. We compare the results from our model to these reference values.

4 RESULTS AND DISCUSSION

The tasks involved fitting the Augmented Lagrangian equation given in Equation 6. The update steps of the optimization algorithm are given in Equation 7, 8 and 9.

Synthetic Data

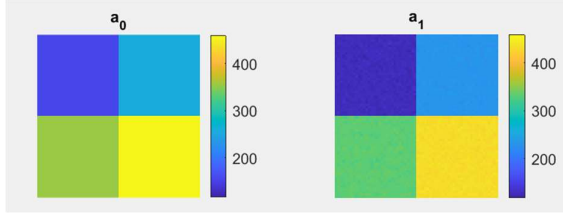


Figure 3: a_0 represents initial signal intensity and a_1 represents signal with Gaussian noise variance=10

We generated synthetic images of 64x64 of different initial intensity values of $a = [155, 255, 355, 455]$.

The estimated images of both a and $T2^* = 1/r$ using our algorithm are given in Figure 4 and Figure 5 and the estimated images of both a and $T2^* = 1/r$ using Levenberg Marquardt are given in Figure 6 and Figure 7

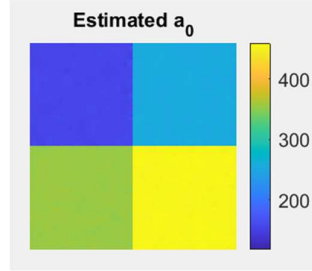


Figure 4: Estimated image of S_0

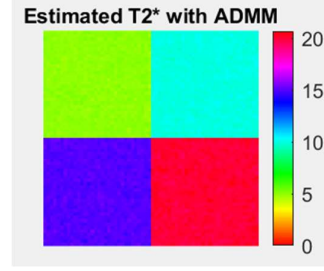


Figure 5: Estimated image of $T2^*$

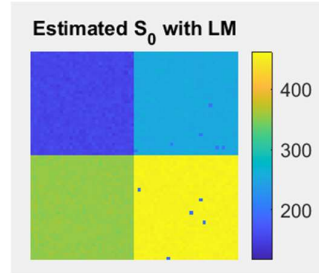


Figure 6: Estimated image of S_0 using LM

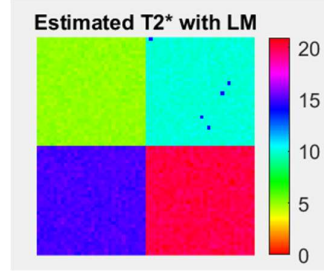


Figure 7: Estimated image of $T2^*$ using LM

Table 1: Comparison of our approach with Levenberg Marquardt for Synthetic Data

S_0	Estimated mean S_0 – Our approach	Estimated mean S_0 using Levenberg Marquardt (Comparison)	Ground truth $T2^*$	Estimated mean $T2^*$ – Our approach	Estimated mean $T2^*$ using Levenberg Marquardt (Comparison)
155	154.9921	154.7440	5	5.0020	5.0134
255	254.9685	254.6956	10	10.0024	10.0247
355	354.9458	354.9451	15	15.0047	15.0070
455	454.8383	453.9505	20	20.0178	19.7594

Total variation (TV) regularization: Assigning total variation regularization functions to the unknown model parameter effectively reduces noise by promoting sparsity in the gradient of the image. From the experiments on the synthetic dataset, we see that in areas where the signal should be constant (homogeneous regions), it smooths out the variations due to noise, resulting in cleaner images. TV should also help to maintain sharp boundaries in the image by penalizing the gradient of the image.

This is necessary in our approach because we have to distinguish between different regions with different iron concentrations within the liver. Since the anatomical structure has distinct edges, TV can lead to a more piecewise-constant reconstruction of the signal

Patient Dataset:

The sequence of MRI images of Patient 1_2 is given in Figure 1.

We notice that the data dimensionality is 192x256

The time to echo(TE) of the data is [2.5800 4.8100 7.5900 9.8900 12.1200 14.3500 16.5800 18.8800]

Due to heterogeneous iron concentration and inclusion of vasculature, T2* measurements can be different in different parts of the liver. However, we take the approximate ROI for the location given as a reference for the dataset as shown in Figure 2.

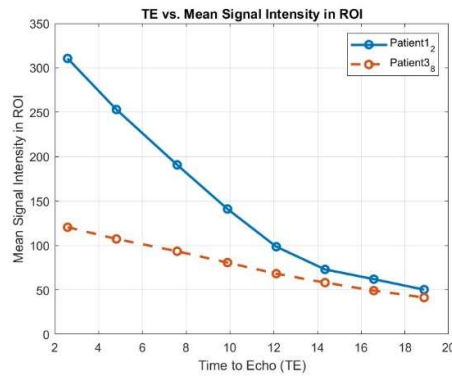
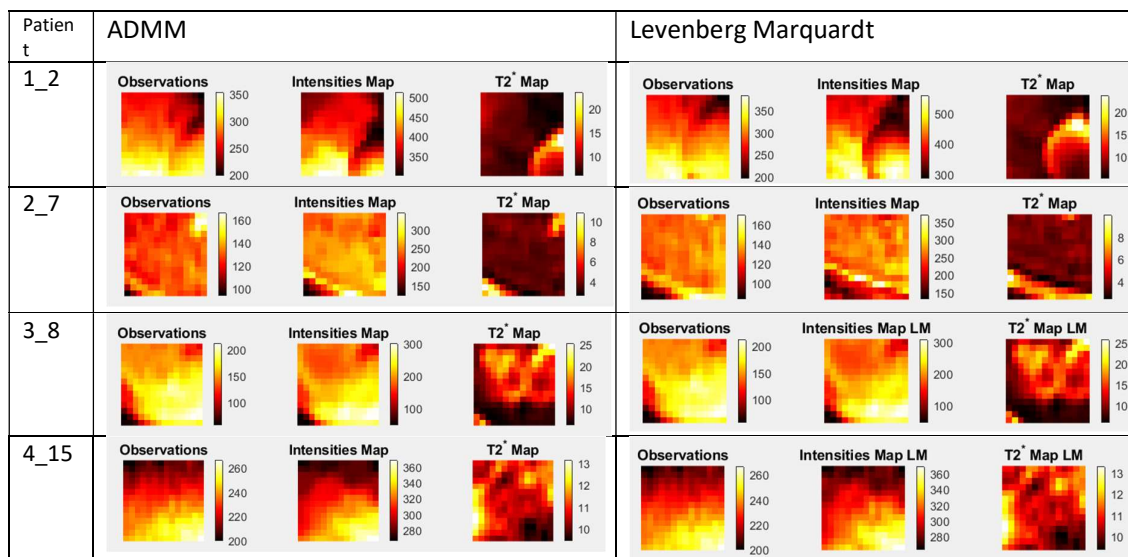


Figure 6: Plot TE versus mean of signal intensity value in the ROI for Patients 1_2 and 3_8

The TE vs mean signal intensity in the ROI for two different patients shows us that both patients show a decrease in mean signal intensity as TE increase. We expect this in T2* imaging because the signal decays exponentially with time due to dephasing of spinning protons in the presence of inhomogeneous magnetic fields. Patient 1's curve starts at a higher intensity and decreases more rapidly than Patient 3's, suggesting a difference in the iron content within the liver. Moreover, we also see a faster decay (steeper slope) indicating higher iron content in the liver for Patient 1_2 compared to patient 3_8, given the more pronounced signal decay

The estimated images of both a and $T2^* = 1/r$ for the patients is shown in Table 2. The Intensities Map reflects the estimated initial signal intensity S_0 . Brighter areas correspond to higher signal intensities, whereas darker areas correspond to lower signal intensities. The T2* maps are indicative of the magnetic properties of the tissue, with the color scale typically representing how quickly the signal from the tissue decays. Darker regions in the T2* map show a shorter T2* relaxation time, which is associated with higher concentrations of iron. However, it's important to note that not all patients adhere to a uniform scale. We also see that the images generated by ADMM and Levenberg Marquardt are very similar for the same ROIs.



The mean T2* value of selected ROI (shown in Figure 2) for each patient using our algorithm is compared with MRI console estimates provided in the folder (Patient Datasets) as well as with the T2* estimated using Levenberg Marquardt. The results are shown in Table 3.

Patients	T2* measurements (console)	Mean T2* (estimated with ADMM) – Our approach	T2* using Levenberg Marquardt (Comparison)
Patient 2_7	9.1323	9.09074	9.100013
Patient 2_7	4.2624	4.140886	4.121563
Patient 3_8	16.2949	12.255314	12.279195
Patient 4_15	10.7012	10.826496	10.832522

The results suggest that our algorithm performs as well as the standard Levenberg Marquardt algorithm and give similar estimates as the reference values from the T2* mapping software integrated into the MRI system.

5 CONCLUSION AND FUTURE WORK

The quantification of liver iron is crucial for early detection, precise staging, and effective monitoring of iron overload in clinical settings. While liver biopsy stands as the gold standard due to its direct assessment of iron levels, it has several practical limitations which limit its widespread applicability. Alternative non-invasive methods like serum biomarkers and CT also have limitations in accuracy and availability. Conversely, MRI emerges as an accessible and non-invasive modality, demonstrating high sensitivity to iron deposits.

This study has successfully developed a model for T2* estimation, leveraging the single exponential model solved by the Alternating Direction Method of Multipliers (ADMM) and Total Variation (TV) to refine parameter estimation. Validation on both synthetic and clinical patient data underscores the model's robustness, with comparative analysis revealing its congruence with established techniques such as the Levenberg-Marquardt algorithm. Integration of this method into clinical protocols could offer a non-invasive and reliable diagnostic tool. In the future, these results should be compared to those from liver biopsy for correctly testing the accuracy of the method.

A limitation of our T2* estimation method is the requirement for manual selection of the Region of Interest (ROI). Currently, the accuracy of ROI placement is critical; if selected improperly, particularly near the liver's edges, the algorithm may fail. Automating this process could mitigate such errors, yet our method maintains manual selection due to variability in MRI scans among patients, which presents a challenge for standardization. Future iterations of this method should focus on developing an adaptive algorithm capable of automated ROI detection that can accommodate the anatomical diversity observed across different individuals.

In related work, the findings of Anderson et al. [8] highlight a compelling direction for research in the management of iron overload, particularly in patients with thalassemia major. Their work raises critical considerations regarding the differential impact of chelation therapies on iron deposition in the liver versus the heart, as they found that myocardial iron levels do not correlate directly with liver iron concentrations. This is important since one of the main causes of patient mortality is cardiac complications which occur due to myocardial iron deposition. Building upon this, future investigations should aim to refine MRI techniques for the simultaneous quantification of iron in both the liver and the heart.

6 REFERENCES

1. Hernando, Diego, et al. "Quantification of liver iron with MRI: State of the art and remaining challenges." *Journal of Magnetic Resonance Imaging*, vol. 40, no. 5, 3 Mar. 2014, pp. 1003–1021, <https://doi.org/10.1002/jmri.24584>.
2. Bondestam, S, et al. "Magnetic resonance imaging of Transfusional Hepatic Iron Overload." *The British Journal of Radiology*, vol. 67, no. 796, 1 Apr. 1994, pp. 339–341, <https://doi.org/10.1259/0007-1285-67-796-339>.
3. Reeder, Scott B., et al. "Quantification of liver iron overload with MRI: Review and guidelines from the ESGAR and sar." *Radiology*, vol. 307, no. 1, 1 Apr. 2023, <https://doi.org/10.1148/radiol.221856>.
4. Ibrahim, El-Sayed H., et al. "Influence of the analysis technique on estimating hepatic iron content using MRI." *Journal of Magnetic Resonance Imaging*, vol. 44, no. 6, 31 May 2016, pp. 1448–1455, <https://doi.org/10.1002/jmri.25317>.
5. Afonso, M V, et al. "An augmented lagrangian approach to the constrained optimization formulation of imaging inverse problems." *IEEE Transactions on Image Processing*, vol. 20, no. 3, Mar. 2011, pp. 681–695, <https://doi.org/10.1109/tip.2010.2076294>.
6. Positano, Vincenzo, Benedetta Salani, Alessia Pepe, et al. "Improved T2* assessment in liver iron overload by magnetic resonance imaging." *Magnetic Resonance Imaging*, vol. 27, no. 2, Feb. 2009, pp. 188–197, <https://doi.org/10.1016/j.mri.2008.06.004>.
7. A. Chambolle, "TV, An Algorithm for Total Variation Minimization and Applications", *J. Math. Imaging Vis.*, vol. 20, pp. 89–97, 2004.

8. Anderson, Lisa J, et al. "Comparison of effects of oral deferiprone and subcutaneous desferrioxamine on myocardial iron concentrations and ventricular function in beta-thalassaemia." *The Lancet*, vol. 360, no. 9332, Aug. 2002, pp. 516–520, [https://doi.org/10.1016/s0140-6736\(02\)09740-4](https://doi.org/10.1016/s0140-6736(02)09740-4).